Modeling of magnetically enhanced capacitively coupled plasma sources: Ar discharges

Mark J. Kushner[a)]
University of Illinois, Department of Electrical and Computer Engineering, 1406 W. Green Street, Urbana, Illinois 61801

Magnetically enhanced capacitively coupled plasma sources use transverse static magnetic fields to modify the performance of low pressure radio frequency discharges. Magnetically enhanced reactive ion etching (MERIE) sources typically use magnetic fields of tens to hundreds of Gauss parallel to the substrate to increase the plasma density at a given pressure or to lower the operating pressure. In this article results from a two-dimensional hybrid-fluid computational investigation of MERIE reactors with plasmas sustained in argon are discussed for an industrially relevant geometry. The reduction in electron cross field mobility as the magnetic field increases produces a systematic decrease in the dc bias (becoming more positive). This decrease is accompanied by a decrease in the energy and increase in angular spread of the ion flux to the substrate. Similar trends are observed when decreasing pressure for a constant magnetic field. Although for constant power the magnitudes of ion fluxes to the substrate increase with moderate magnetic fields, the fluxes decreased at larger magnetic fields. These trends are due, in part, to a reduction in the contributions of more efficient multistep ionization. © *2003 American Institute of Physics.* [DOI: 10.1063/1.1587887]

I. INTRODUCTION

Magnetically enhanced capacitively coupled radio frequency (rf) plasma sources have been developed for the high plasma density etching and sputtering of materials for microelectronics fabrication.[1–6] In this application the devices are often called magnetically enhanced reactive ion etching (MERIE) reactors. A typical MERIE reactor is a parallel plate device operating at tens to hundreds mTorr of gas pressure and few to tens MHz excitation frequency. A static magnetic field is usually applied parallel to the electrodes with the goal of increasing the plasma density for a given power deposition by reducing the rate of loss of charged particles. Due to the difficulty of obtaining tailored magnetic fields across large wafers, MERIE reactors often use rotating static magnetic fields to average out nonuniformities resulting from $\mathbf{v} \times \mathbf{B}$ forces.[1] The sensitivity of plasma uniformity on the configuration of the magnetic field was demonstrated by Buie *et al.*[7] who correlated the uniformity of SiO_2 etching at low pressure with the gradient of the static magnetic field. Through experiment and modeling, Paranjipe *et al.*[8] showed that by adjusting the lateral distribution of the magnetic field by use of iron field pieces, the plasma density in a MERIE reactor could be controlled from being center high to edge high.

MERIE reactors have been used for microelectronics fabrication for many years with there being few quantitative experimental or modeling studies reported in the open literature. Yeom *et al.*[9,10] made electric probe measurements of plasma potential and ion density in a cylindrical MERIE in a magnetron configuration sustained in argon with different diameter powered electrodes. Due to the large area ratio, in the absence of a magnetic field the dc bias was as large as 0.9 of the amplitude of the rf bias. For a gas pressure of 3 mTorr, the dc bias decreased (became less negative) with increasing magnetic field, indicating that more current, on a relative basis, was being collected at the powered electrode. The phase angle between the current and voltage also decreased from $\approx 85°$ without the magnetic field to $45°–60°$ at 200 G, indicating a more resistive plasma. These trends may be partially explained by the decrease in cross field electron mobility with increasing magnetic field and a larger proportion of the current being carried by ions. They also found that the ion density transitions to being essentially uniform across the gap without a magnetic field to being highly peaked near the powered electrode as the magnetic field increases. These results suggest that the confinement is more effective for higher energy sheath heated or secondary electrons which are largely responsible for ionization. The decrease in dc bias may partly result from localization of those ionization sources near the powered electrode.

The transition to a more resistive plasma with increases in the magnetic field was quantified by Hutchinson *et al.*[11] who performed particle-in-cell simulations of a MERIE sustained in 10 mTorr Ar with a 7.5 cm gap and magnetic fields of 0–60 G. With small magnetic fields (10 G) the dominant mode of electron heating changed from stochastic to collisional (ohmic) accompanied by a decrease in electron density. This transition was accompanied by an increase in the bulk electron temperature, indicating a less efficient ionization mechanism. At larger magnetic fields the plasma density increased while the bulk electron temperature did not appreciably change. Avtaeva *et al.*[12] performed diagnostics of MERIE reactors operating in Ar and CH_4 over a range of pressures of 0.7–70 mTorr and magnetic field strengths of 0–200 G. For discharges in 10 mTorr Ar, the electron density

[a)]Electronic mail: mjk@uiuc.edu

increased roughly linearly with magnetic field, whereas the electron temperature increased from 3.2 to 5.1 eV.

Park and Kang[13] developed a magnetic sheath model with which they investigated scaling laws in MERIE reactors. They found that in the absence of a magnetic field, the plasma density increased linearly with pressure over the range of 10 mTorr–1 Torr. With magnetic fields up to 100 G, plasma densities were nearly constant starting with lower pressures until reaching the no magnetic field plasma density at higher pressures. The pressure at which this match occurred increased with increasing magnetic field, as the larger collision frequency at the higher pressure competed with the confinement provided by the decreasing Larmor radius at higher magnetic fields.

These trends were also observed in models and experiments by Lieberman *et al.*[14] Using a magnetic sheath model coupled to a global discharge model, they found that the dc bias decreased (became less negative) with increasing magnetic field (10–100 G) with the effect being most prominent at lower pressures (10 mTorr) while being nominal at higher pressures (100 mTorr). Measurements in a commercial MERIE reactor validated these trends.

In this article, results of a computational investigation of a MERIE reactor having plasmas sustained in Ar are presented. Systematic trends for ion flux, electron temperature and dc bias are discussed for a MERIE reactor resembling an industrial design. For constant power, we found that the dc bias decreased (became less negative) with increasing magnetic field in large part due to more efficient confinement of ionization sources near the powered electrode, particularly those from to secondary electrons, and due to the decrease in electron mobility relative to the ions. The spatial distribution of the plasma is also sensitive to the magnitude of the magnetic field, in this geometry transitioning from edge high to center high to uniform with increasing magnetic field. Ion fluxes to the substrate reflect the change in bias, decreasing in energy and broadening in angle as the magnetic field increases. These trends also result from a reversal in the electric field in the sheath during the anodic portion of the rf cycle and a thickening of the sheath producing more collisional conditions for ion transport. The model used in this study is discussed in Sec. II. Parametric results from our investigation of properties of argon plasmas sustained in a MERIE are presented in Sec. III. Concluding remarks are in Sec. IV.

II. DESCRIPTION OF THE MODEL

The model used in this investigation is a fluid hydrodynamics simulation augmented by a Monte Carlo simulation (MCS) for secondary electrons. Continuity, momentum and energy equations for neutrals and ions; continuity and energy equations for electrons and Poisson's equation for the electric potential are integrated in time to obtain a periodic steady state. The resulting electric fields and ion fluxes to surfaces are periodically transferred to the MCS where the transport of secondary electrons emitted from surfaces is addressed. Electron impact source functions and sources of secondary electron current resulting obtained from the MCS are

returned to the fluid model. The process is iterated to convergence. Although the results discussed here are for Ar plasmas, results for more complex gas mixtures will be discussed in a subsequent publication. The description of the model is therefore presented in the context of a multicomponent gas mixture.

The equations solved for neutral and ion transport (continuity, momentum and energy) are

$$\frac{\partial N_i}{\partial t} = -\nabla \cdot \boldsymbol{\phi}_i + S_i - \left[\sum_j \gamma_{ij}(\nabla \cdot \boldsymbol{\phi}_j) \right]_S, \tag{1}$$

$$\frac{\partial \boldsymbol{\phi}_i}{\partial t} = \frac{\partial (N_i \mathbf{v}_i)}{\partial t}$$

$$= -\frac{1}{m_i} \nabla (k N_i T_i) - \nabla \cdot (N_i \mathbf{v}_i \mathbf{v}_i) + \frac{q_i N_i}{m_i}$$

$$\times (\mathbf{E} + \mathbf{v}_i \times \mathbf{B}) - \nabla \cdot \bar{\bar{\mu}}_i - \sum_j \frac{m_j}{m_i + m_j}$$

$$\times N_i N_j (\mathbf{v}_i - \mathbf{v}_j) \nu_{ij} + \mathbf{S}_{mi}, \tag{2}$$

$$\frac{\partial (N_i \varepsilon_i)}{\partial t} = -\nabla \cdot \bar{\bar{\kappa}} \nabla T_i - P_i \nabla \cdot \mathbf{v}_i - \nabla \cdot (N_i \mathbf{v}_i \varepsilon_i) + q_i \boldsymbol{\phi}_i \cdot \mathbf{E}$$

$$-(\bar{\bar{\mu}} \cdot \nabla \mathbf{v}_i) - \sum_{m,j} k_{mij} N_j N_i \varepsilon_i$$

$$+ \sum_{m,j,l} k_{mjl} N_j N_l \Delta \varepsilon_{mjl}, \tag{3}$$

where $\boldsymbol{\phi}_i$ is the flux of species i having density N_i, velocity $\mathbf{v}_i$, mass m_i, temperature T_i, viscosity μ_i, pressure P_i, and total energy ε_i. S_i is the source for species i due to gas phase collision processes, ν_{ij} is the momentum transfer collision frequency between species i and j, and $\bar{\bar{\kappa}}$ is the thermal conductivity which, in the case of charged species, has tensor form as discussed below. $\mathbf{E}$ is the electric field and $\mathbf{B}$ is the static applied magnetic field. Temperature jump boundary conditions are employed using the method described in Ref. 15. Heavy particle neutral transport coefficients are derived from Lennard-Jones potentials, also described in Ref. 15.

In Eq. (1), the last term accounts for the consumption and production of species on surfaces, where γ_{ij} is the coefficient for production of species i by reactions of species j on a surface. Computationally, we assume all species are consumed with unity probability on surfaces, implemented in the first term of Eq. (1) by having a zero density on the surface. If a species is unreactive it is "replaced" at the boundary by specifying a flux returning to the plasma having the same magnitude as incident onto the surface. For example, $\gamma_{ii} = 1.0$ for species having a zero reactive sticking coefficient. S_i contains contributions from electron impact reactions resulting from secondary electrons as obtained from the MCS. In the case of electrons, this contribution also includes the slowing of beam electrons into the bulk distribution and so represents the injected negative charge from secondary emission.

In Eq. (2), S_{mi} is the rate of generation and loss of momentum for species i resulting from collisions which change the identity of the reactant. These are collisions other than elastic momentum transfer collisions which are accounted for by the term containing ν_{ij}. For example, a process progressing at rate r (1/s) which produces species i from species j (as in a charge exchange) has $\mathbf{S}_{mi}=rN_j\mathbf{v}_j$. Effects such as cataphoresis are captured by the term for momentum transfer between ions and neutrals. Since viscous forces are negligible for ions for our conditions, that term is not included for charged species when solving Eq. (2). Slip boundary conditions are implemented using the method described by Thompson.[16] In that method, the velocity at and parallel to a surface is given by

$$v_p = \frac{1+\beta}{1-\beta}\lambda\left(\frac{dv_p}{dy}\right),$$

where λ is the collisional mean free path and β is the fraction of parallel velocity retained on a collision with a surface.

A separate total energy for each species is tracked based on the solution of Eq. (3). Our definition of total energy is the sum of directed and random translational energy. As such, we include power transfer by thermal conductivity, compressive heating, advective transport, Joule heating, and viscous dissipative heating for each species on an individual basis. The method for accounting for the change in enthalpy is somewhat non-conventional, and is accounted for by the last two terms of Eq. (3). All reactions m of species i with species j having rate coefficient k_{mij} which results in removal of species i produces a loss of total energy for species i of ε_i per event. All reactions m between species j and l which produce species i, including elastic collisions, provides for a unique contribution to the total energy of $\Delta\varepsilon_{mjl}$ per event. For example, the electron impact reaction $e+\mathrm{Ar}\rightarrow\mathrm{Ar}^++e+e$ makes a contribution of only $\varepsilon(\mathrm{Ar}^+)$, that is the translational energy of Ar^+ and not the total change in enthalpy difference between Ar and Ar^+ because we track the energy of each species separately. For reactions such as $e+\mathrm{O}_2\rightarrow\mathrm{O}+\mathrm{O}+e$ we include the translational and Frank–Condon heating contributions. Heavy particle chemical reactions would include the appropriate exothermicities.

The electron flux is given by

$$\boldsymbol{\phi}_e = qn_e\bar{\bar{\mu}}_e\cdot\mathbf{E}-\bar{\bar{D}}_e\cdot\nabla n_e, \tag{4}$$

where $\bar{\bar{\mu}}_e$ and $\bar{\bar{D}}_e$ are the tensor mobility and diffusivity. The tensor forms of transport coefficients, $\bar{\bar{A}}$ are derived from their isotropic values, A_0 by

$$\bar{\bar{A}} = \frac{A_0}{(\alpha^2+|\mathbf{B}|^2)}$$

$$\times\begin{pmatrix} \alpha^2+B_r^2 & \alpha B_z+B_r B_\theta & -\alpha B_\theta+B_r B_z \\ -\alpha B_z+B_r B_\theta & \alpha^2+B_\theta^2 & \alpha B_r+B_\theta B_z \\ -\alpha B_\theta+B_r B_z & -\alpha B_r+B_\theta B_z & \alpha^2+B_z^2 \end{pmatrix},$$

$$\alpha = \frac{\nu_m m}{q}, \tag{5}$$

where ν_m is the electron (or ion) momentum transfer collision frequency.

Power transport of bulk electrons is addressed by time integration of the electron energy equation

$$\frac{\partial(\frac{3}{2}n_e kT_e(\mathbf{r}))}{\partial t} = P(\mathbf{r})-L(T_e)$$

$$-\nabla\cdot\left(\frac{5}{2}\boldsymbol{\phi}_e kT_e-\bar{\bar{\kappa}}(T_e)\cdot\nabla T_e\right)+P_{\mathrm{EB}}(\mathbf{r}), \tag{6}$$

where $\bar{\bar{\kappa}}$ is the tensor thermal conductivity, P is the power deposition from the electrostatic field, P_{EB} is the power transferred from slowing beam electrons (and their progeny) to the bulk distribution, and L is the power loss due to collisions. The electrostatic heating is given by collisional Joule heating $P(\mathbf{r})=q_e\boldsymbol{\phi}_e\cdot\mathbf{E}$ and so ignores the stochastic component. Isotropic transport coefficients and electron impact rate coefficients were obtained from solution of Boltzmann's equation using a two-term spherical harmonic expansion approximation.[17]

The time rate of change in charge density ρ_m on surfaces and in materials is given by

$$\frac{\partial\rho_m(t)}{\partial t} = \left[-\sum_i q_i(\nabla\cdot\boldsymbol{\phi}_i(t))-\sum_{i,j} q_j(\nabla\cdot\boldsymbol{\phi}_i(t)\gamma_{ij})\right]_s$$

$$+[\nabla\cdot\sigma\nabla\Phi]_m, \tag{7}$$

where Φ is the electric potential, σ is the conductivity of a nonplasma material, and γ_{ij} is the secondary emission coefficient for species j by species i. The first term applies to only locations on surfaces in contact with the plasma while the second term applies to points in and on nonplasma materials.

Poisson's equation for the electric potential is solved using a modified form of the semi-implicit technique described in Ref. 18. The potential at time $t+\Delta t$ is obtained from

$$\nabla\cdot\varepsilon\nabla\Phi(t+\Delta t) = -\left\{\rho_m(t)+\sum_i q_i N_i(t)\right.$$

$$+\Delta t\cdot\left[\frac{\partial\rho_m(t')}{\partial t}-q_e\nabla\cdot\phi_e(t')\right.$$

$$\left.\left.-\sum_j q_j\nabla\cdot\left(\phi_j(t)+\frac{\Delta t}{2}\frac{\partial\phi_j(t)}{\partial t}\right)\right]\right\}, \tag{8}$$

where ε is the local permittivity. The terms in Eq. (8) are for the accumulation of charge on surfaces and in the bulk plasma at the present time, and prediction of such charges at the future time. ρ_m and N_i are evaluated at t, while t' denotes that densities are evaluated at t and potentials are evaluated at $t+\Delta t$, thereby providing implicitness. The implicitness of the solution is largely achieved through the dependence of the electron flux on the electric potential. The sum over j includes only ions. In prior works, the flux of ions, on any given solution of Eq. (8), was given by the solution of Eq. (2) from the previous time step and was held constant during solution of Eq. (8). We found that for the

magnetic fields of interest here (100's G), the Lorentz force is large enough to introduce nonlinearity into the ion transport, making the constant flux assumption poor. To address this nonlinearity, the second term in Taylor's expansion for the ion density was included by numerically deriving the time rate of change of the ion flux. Due to short wavelength (high spatial frequency) properties of Eq. (8) when including the magnetic fields, previously used iterative techniques such as successive over relaxation were insufficient for its solution. Instead, we used an incomplete LU biconjugate gradient sparse matrix technique.[19]

Secondary electron emission from surfaces is addressed using the MCS. The electric fields produced in the fluid module are binned according to position and phase in the rf cycle, the ion fluxes to surfaces are averaged over the rf cycle, and these quantities are transferred to the MCS. In the MCS, electron pseudoparticles are released from surfaces with an energy of 4 eV at random times during the rf cycle and are weighted by the magnitude of the local ion flux and the secondary electron emission coefficient. The weighting of each pseudoparticle has units of electrons/s. Using the techniques described in Ref. 20, the trajectories of the secondary beam electrons and their progeny are integrated as a function of time. Pseudoparticles (and their progeny) are tracked until they hit boundaries or fall below a specified energy thereby joining the bulk electron distribution, at which time their weightings are summed into S_i for electrons. Sampling of the trajectories and binning of the pseudoparticles produces a time averaged, spatially dependent electron energy distribution, $f(\varepsilon, \mathbf{r})$ having units of electrons cm^{-3} eV^{-1}. When convolved with electron impact cross sections, source functions having units cm^{-3} s^{-1} are produced which then contribute to S_i for the appropriate species.

The energy and angular distributions of ions and neutrals incident on the substrate are obtained using a heavy particle MCS.[21] Electric fields binned by position and phase in the rf cycle are used to advance the trajectories of pseudoparticles representing neutrals and ions. To account for generation and loss of particles, all processes which produce an ion i, are summed to yield a spatially dependent source function S_{1i}. Similarly, all processes which consume ion i are summed to yield a spatially dependent sink function S_{2i}. The rate of elastic collisions is summed into a third source function S_{3i}. Finally, a null collision rate S_{ni} is chosen for every spatial location so that the total collision rate is constant at $S_{Ti} = S_{2i} + S_{3i} + S_{ni}$. Reactions in which species are produced with unique momenta, such as charge exchange, are separately tracked. Pseudoparticles are launched at random phases in the rf cycle from spatial locations in proportions given by S_{1i}. The time to the next collision is chosen by $\tau = (-1/S_{Ti}) \ln(r_1)$, where r_1 is a random number distributed (0,1). The trajectory of the pseudoparticle is integrated for a time τ. At the collision site, a series of random numbers is chosen to determine the fate of the particle. If $r_2 < S_{ni}/S_{Ti}$, the collision is null, and a new trajectory is started. If not null another random number is chosen to determine if the collision is elastic or identity changing. If $r_3 < S_{2i}/(S_{2i} + S_{3i})$, the collision is elastic. Through a sequence of ran-
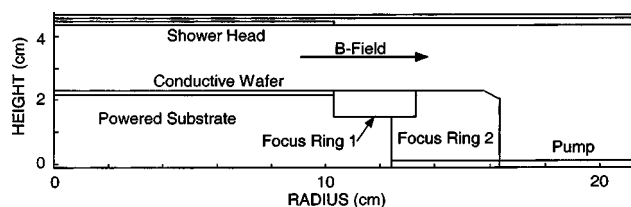

FIG. 1. Schematic of the MERIE geometry used in this study. The magnetic field is purely radial.

dom numbers, the collision partner is selected and the velocity adjusted appropriate with a momentum transfer encounter. If the collision is identity changing, the particle is removed from the simulation. The exception is a charge exchange collision where the momentum of the incoming ion is stored for launching of a hot neutral pseudoparticle.

The trajectories of the pseudoparticles are tracked until they enter the presheath near a surface, and the identity of the surface the pseudoparticle will strike is clear. If statistics are not desired for ion fluxes striking that surface, the pseudoparticle is removed from the simulation to avoid the computationally expensive task of advancing the trajectory through the sheath. Otherwise, the trajectory of the pseudoparticle is integrated across the sheath, binning its energy and angle when it strikes the surface.

III. PLASMA PROPERTIES IN MERIE REACTORS

The model reactor used in this study, shown schematically in Fig. 1, is patterned after plasma sources which are commercially available. The metal substrate is powered at 10 MHz through a blocking capacitor. A conductive Si wafer ($\sigma = 0.01/\Omega$ cm), 20 cm in diameter, sits in electrical contact with the powered substrate which is surrounded by a Si ring ($\varepsilon/\varepsilon_0 = 12.5$, $\sigma = 10^{-6}/\Omega$ cm) and dielectric focus ring ($\varepsilon/\varepsilon_0 = 8.0$, $\sigma = 10^{-6}/\Omega$ cm). All other surfaces in the reactor are grounded metal including the showerhead, which extends to a radius of 10 cm, and the annular pump port. The base case operating conditions are 40 mTorr of Ar with a flow rate of 300 sccm. The reaction mechanism for Ar is discussed in Ref. 18.

As this is a two-dimensional, cylindrically symmetric simulation, we are unable to address the true asymmetries and cross-wafer magnetic fields of industrial devices. As an approximation to these fields, we specified that the magnetic field be purely radial and parallel to the electrodes. Although this magnetic field is unphysical at $r=0$, it is the configuration which best captures, within available computing resources, the behavior produced by asymmetric cross-wafer magnetic fields. The following test was conducted to confirm that the radial magnetic field does indeed capture the behavior of cross-wafer fields. Simulations were performed in a two-dimensional Cartesian geometry for the entire reactor. A unidirectional magnetic field parallel to the substrate was imposed, approximating the asymmetric magnetic fields of industrial reactors. Qualitatively and quantitatively similar trends were obtained as when using the cylindrical geometry
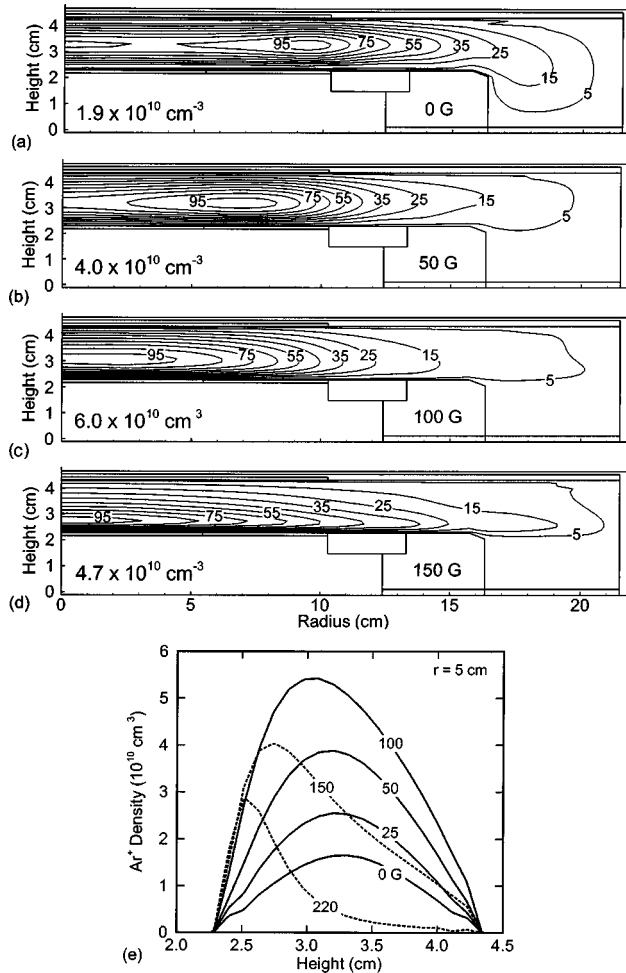
FIG. 2. Time averaged argon ion density for 100 W, 40 mTorr discharges for increasing magnetic field strength: (a) $B=0$, (b) $B=50$ G, (c) $B=100$ G, (d) $B=150$ G, and (e) ion density as a function of height at $r=5$ cm. The contours are labeled with the percentage of the maximum value indicated in each frame. The rf voltage amplitude was adjusted to maintain constant power. With increasing magnetic field, the maximum in ion density shifts towards the center of the reactor and towards the substrate.
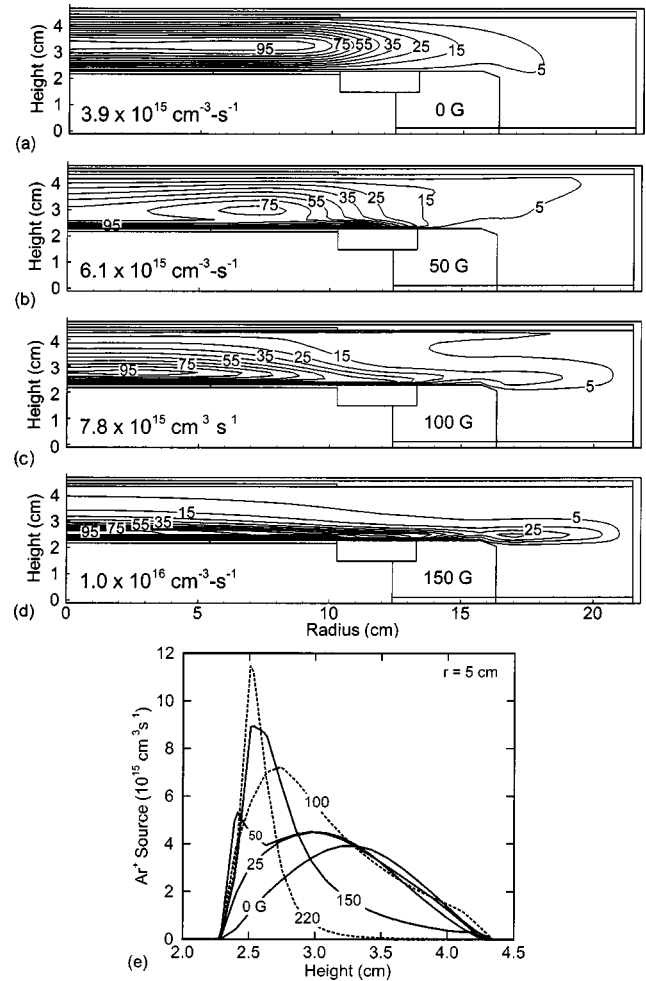
FIG. 3. Time averaged ionization source by bulk electrons for 100 W, 40 mTorr discharges for increasing magnetic field strength: (a) $B=0$, (b) $B=50$ G, (c) $B=100$ G, (d) $B=150$ G, and (e) ionization source as a function of height at $r=5$ cm. The contours are labeled with the percentage of the maximum value indicated in each frame. With increasing magnetic field, the ionization source is increasingly confined to the vicinity of the substrate.

having a radial magnetic field, but at the cost of doubling the computational workload to maintain the same spatial resolution.

The Ar^+ density as a function of position is shown in Fig. 2 for a power deposition of 100 W and magnetic fields of 0–150 G. The corresponding ionization sources by bulk electrons are shown in Fig. 3 and the bulk electron temperatures are shown in Fig. 4. The rf voltage amplitude was adjusted to maintain constant power. In the absence of a magnetic field, the maximum ion density is 1.9×10^{10} cm^{-3}, supported by an electron temperature of 4.5 eV in the middle of the gap. Due to the high plasma density and resulting thin sheath thickness, the time averaged electron density is nearly indistinguishable from the ion density on the scale of Fig. 3. The ion density is radially uniform over the inner two thirds of the wafer to better than 10%, with there being a maximum near the edge of the wafer, characteristic of narrow gap, capacitively coupled discharges.[22] As the electron temperature is fairly uniform due to the large electron thermal conductivity at this comparatively low pressure, the ionization source closely mirrors the electron density.

With an increase in magnetic field there is a systematic shift in the maximum of the ion density towards the powered electrode, as observed experimentally,[9] and towards the center of the reactor. This shift is produced by a corresponding shift in the source of ionization by bulk electrons and in the electron temperature, though the shift in T_e is smaller in comparison. The maximum in the ionization source monotonically increases as the magnetic field increases up to 200 G. The peak ion density and ion flux have maxima as a function of magnetic field, as shown in Fig. 5. The maximum ion density increases up to 100 G, decreasing thereafter, while the ion flux to the center of the wafer shows a similar trend with the maximum flux occurring at 150 G.

The trends in electron temperature and bulk ionization source are largely explained by the decrease in the axial mobility and thermal conductivity of electrons with increasing magnetic field. The electron Larmor radius and cyclotron frequency at 100 G are 0.6 mm and 2.8×10^8 s^{-1}, whereas the sheath thickness and electron momentum transfer collision frequency are ≈ 1 mm and 1.8×10^8 s^{-1}. As the magnetic field approaches and exceeds 100 G, the cyclotron fre-
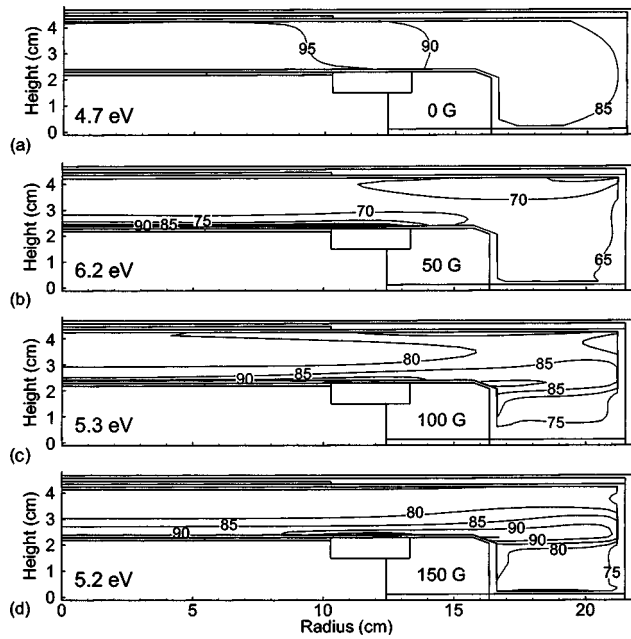
FIG. 4. Time averaged bulk electron temperature 100 W, 40 mTorr discharges for increasing magnetic field strength: (a) $B = 0$, (b) $B = 50$ G, (c) $B = 100$ G, and (d) $B = 150$ G. The contours are labeled with the percentage of the maximum value indicated in each frame. The decrease in electron cross field mobility and thermal conductivity produces peaks in electron temperature near the powered substrate. As longitudinal transport is unaffected, lobes of high electron temperature occur in the periphery of the reactor.

quency increases above the momentum transfer collision frequency and the Larmor radius falls below the sheath thickness, thereby limiting the axial convection of electron energy and confining the peak electron temperature to the site of maximum power deposition at the sheath edge. As the parallel component of electron heat conduction is unaffected by the magnetic field, electron thermal energy convects laterally, producing lobes of higher temperature in the periphery of the reactor. This confinement and lateral convection of
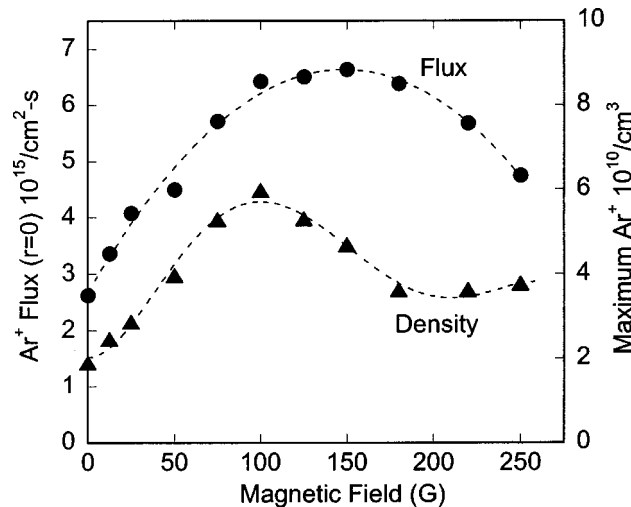

FIG. 5. Ion flux to the center of the substrate and maximum ion density as a function of magnetic field strength (100 W, 40 mTorr). The ion flux has a maximum at an intermediate magnetic field.
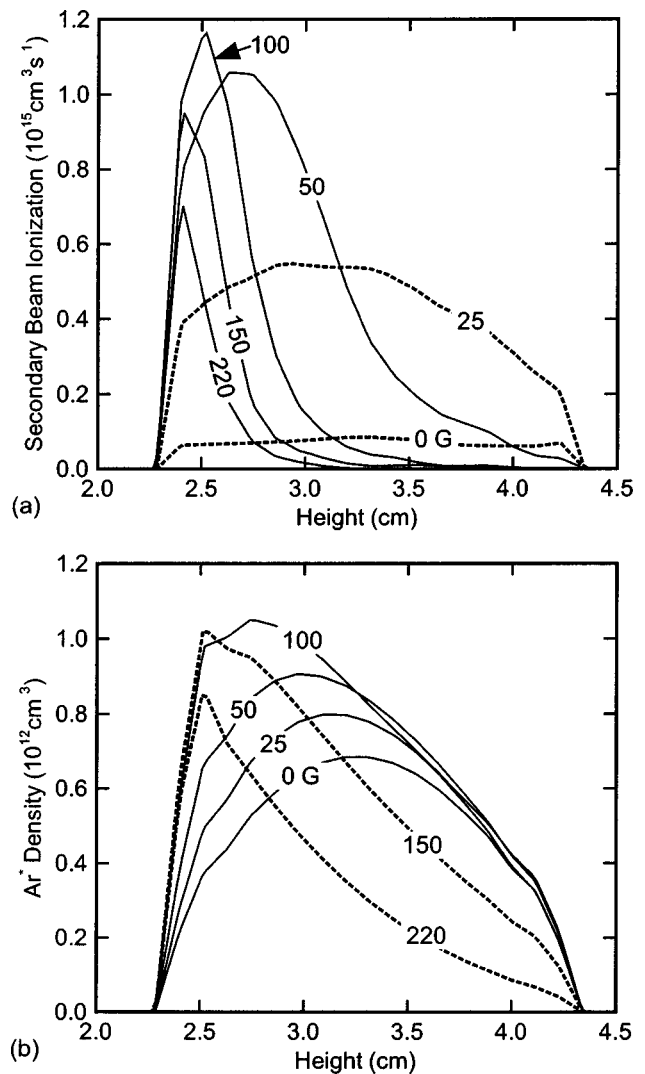

FIG. 6. Plasma properties as a function of height in the reactor at a radius of 5 cm (100 W, 40 mTorr); (a) ionization source by secondary beam electrons and (b) Ar(4s) density. The curves are labeled with the value of the magnetic field (G). Increasing magnetic field localizes ionization sources closer to the substrate. The Ar(4s) density has a corresponding shift which ultimately reduces its value due to increased rates of diffusion loss.

electron power in turn confines the ionization source to be closer to the substrate and to have lobes in the periphery of the reactor.

The shift in the peak ion density towards the substrate is in part facilitated by the confinement of the beam electrons resulting from secondary electron emission. The ionization sources resulting from the beam electrons are shown in Fig. 6 as a function of height at a radius of 5 cm for magnetic fields up to 220 G. Without a magnetic field, the rf amplitude is 130 V and dc bias is -16 V, producing secondary electrons having maximum energies of about 150 eV. These electrons have mean free paths of about 2 cm, nearly the same as the interelectrode gap of 2.1 cm. The ionization source from beam electrons is therefore fairly uniform across the gap and a large proportion of the secondary electron flux is lost to the opposite grounded electrode. As the magnetic field increases to tens of G and the Larmor radius decreases, the ionization source due to beam electrons is more efficiently utilized. For

example, for $B = 25$ G the Larmor radius for 150 eV electrons is 1.7 cm, thereby ideally confining the secondary electrons to dissipate their energy within the 2.1 cm gap. This increases the beam ionization source throughout the gas, as shown in Fig. 6. Further increases in magnetic field confine the beam electrons closer to the powered electrode, resulting in the loss of emitted electrons which are returned to and collected by the electrode. A decrease in the peak ionization rate and poorer utilization of the beam electrons result. For example, the rate of ionization by beam electrons peaks at about 25% of the bulk rate at $B = 50$ G and proportionally decreases at higher magnetic fields.

The decrease in ion density and flux at large magnetic fields can be attributed to at least two second order effects; multistep ionization and the dependence of dc bias on magnetic field. Just as the ionization source is confined to be closer to the powered electrode as the magnetic field increases, so is the excitation rate of electronic states. In particular, the source of excitation for Ar($4s$) metastables is confined to be closer to the electrode, producing a shift in the peak density of Ar($4s$) towards the powered substrate, as shown in Fig. 6. As the transport of neutral species in unaffected by the magnetic field, the confinement of the excitation rate of Ar($4s$) not only shifts the peak in its density towards the substrate but also results in an increase in its rate of loss by diffusion to the substrate. The final outcome is a decrease in the Ar($4s$) density and a corresponding decrease in the fractional contribution of the more efficient ionization of Ar($4s$) to the total ionization rate. This reduction in a highly efficient ionization mechanism reduces the electron density. For example, without a magnetic field, the electron impact ionization of Ar($4s$) and Penning ionization of Ar($4s$) are responsible for 21% and 6% of the total ionization. With a magnetic field of 250 G, these contributions are only 10% and 2%.

The second contributing cause to the reduction in ion flux is the behavior of the rf amplitude and dc bias. While varying the magnetic field, the total power deposition was held constant at 100 W by adjusting the rf voltage. The resulting rf amplitude and dc bias are shown in Fig. 7 as a function of magnetic field. With a small increase in magnetic field (<30 G) the dc bias increases (becomes more negative). The powered substrate collects only cross field current while the grounded surfaces collect both cross field and parallel current. The decrease in cross field mobility by moderate magnetic fields more detrimentally affects the ability of the substrate to collect current than the opposing electrode, thereby producing a more negative dc bias to compensate. However for larger magnetic fields, the localization of ionization sources near the powered electrode increases its current collecting capability relative to the grounded electrode, while the decrease in electron mobility relative to the ions results in a larger proportion of the current being carried by ions. The dc bias becomes more positive to compensate, reaching 40 V for $B = 250$ G. As the transverse electron mobility decreases with increasing magnetic field, the discharge becomes more resistive and the rf amplitude increases. At the largest magnetic fields investigated (250–300 G), the ions also begin to become magnetized (the ion Larmor radius is 2
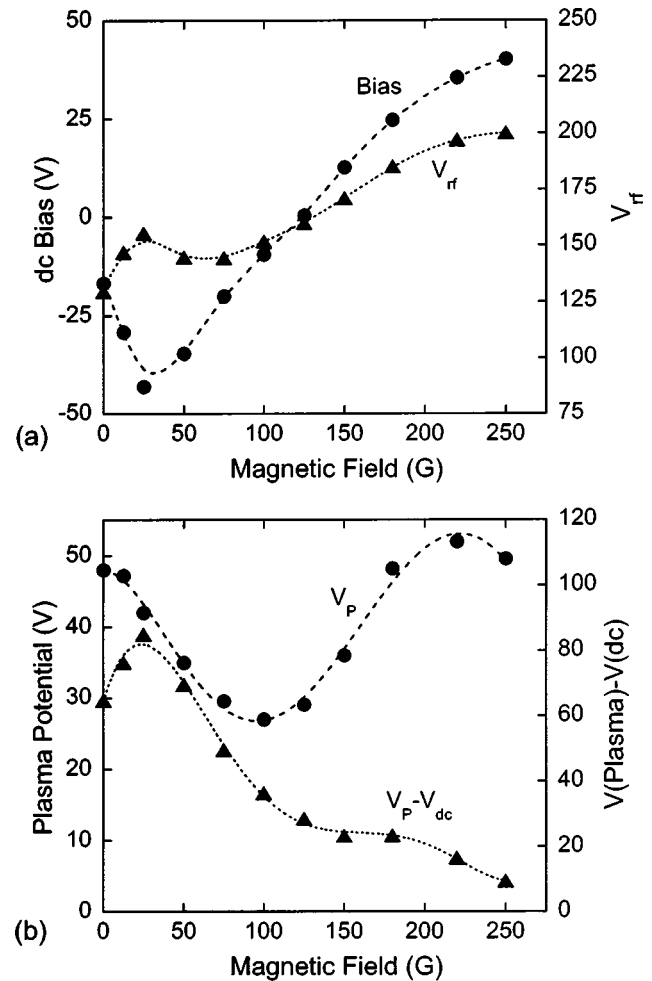

FIG. 7. Electrical properties as a function of magnetic field (100 W, 40 mTorr): (a) dc bias [V_{dc}] and rf voltage amplitude and (b) time averaged plasma potential V_P and V_P-V_{dc}.

cm at 250 G) and so contribute to the increase in resistivity.

The maximum secondary electron energy due to emission from the powered electrode is in part determined by the difference in the maximum plasma potential and dc bias, V_P-V_{dc}. Although the increase in the rf amplitude and dc bias are such that the difference V_{rf}-V_{dc} is approximately the same (160 V) as the magnetic field is increased, the dynamics of the discharge are such that the time averaged value of V_P-V_{dc} decreases. These dynamics are largely a consequence of the electron mobility decreasing, resulting in a larger proportion of current being carried by the ions as the magnetic field increases. For example, the ratio of the electron to ion cross field mobilities, μ_e/μ_I, at 40 mTorr for $B = 0$, 75, 150, and 225 G are approximately 350, 4, 1, and 0.5. The more resistive plasma has a larger voltage drop across the bulk plasma and proportionally less across the sheath. For example, the time average values of V_P-V_{dc} at a $r = 5$ cm is shown in Fig. 7 as a function of magnetic field. (The time averaged plasma potential is a weak function of radius.) The decrease in V_P-V_{dc} produces less energetic secondary electrons having a shorter range producing a smaller ionization source. Although a small decrease in secondary electron en-
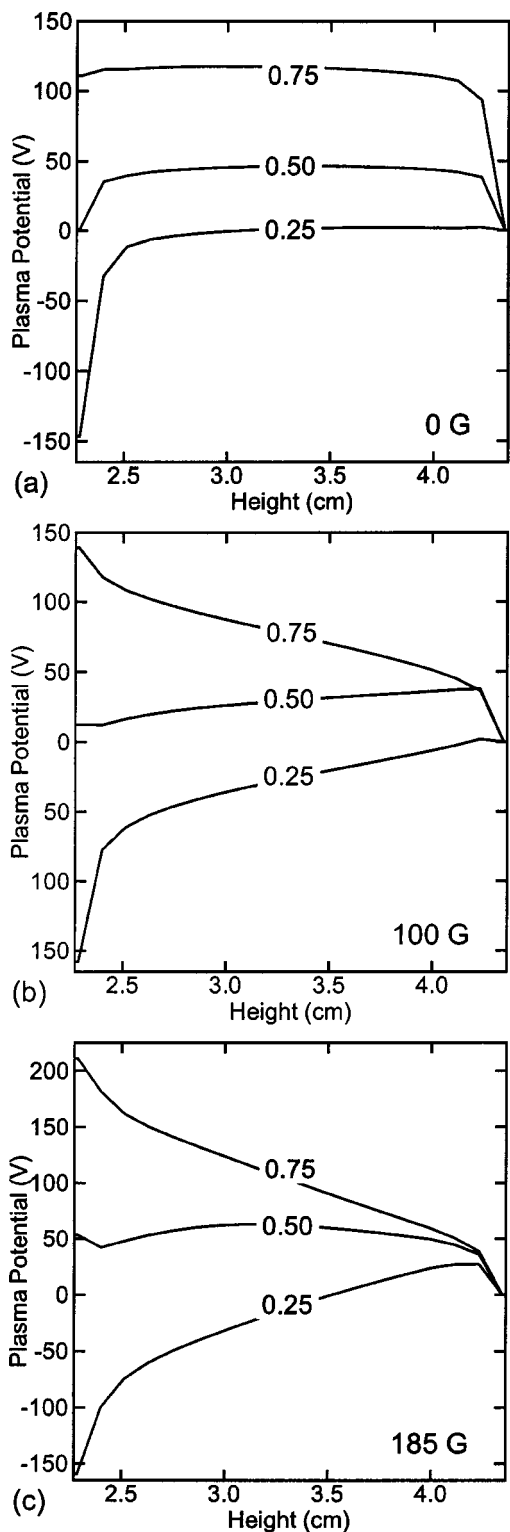
FIG. 8. Plasma potential as a function of height at radius $r = 5$ cm at different fractional phases during the rf cycle (100 W, 40 mTorr): (a) $B = 0$ G, (b) $B = 100$ G, and (c) $B = 185$ G. The fraction phases of 0.25 and 0.75 correspond to the cathodic and anodic peaks. With increasing magnetic field, the plasma becomes more resistive and less electropositive, culminating in a reversal of the electric field in the powered sheath.

ergy is beneficial to slow the electrons in the gap, the degree of decrease here results in a net lowering of the ionization rate.

The consequences of the decrease in electron cross field mobility with increasing magnetic field are demonstrated by
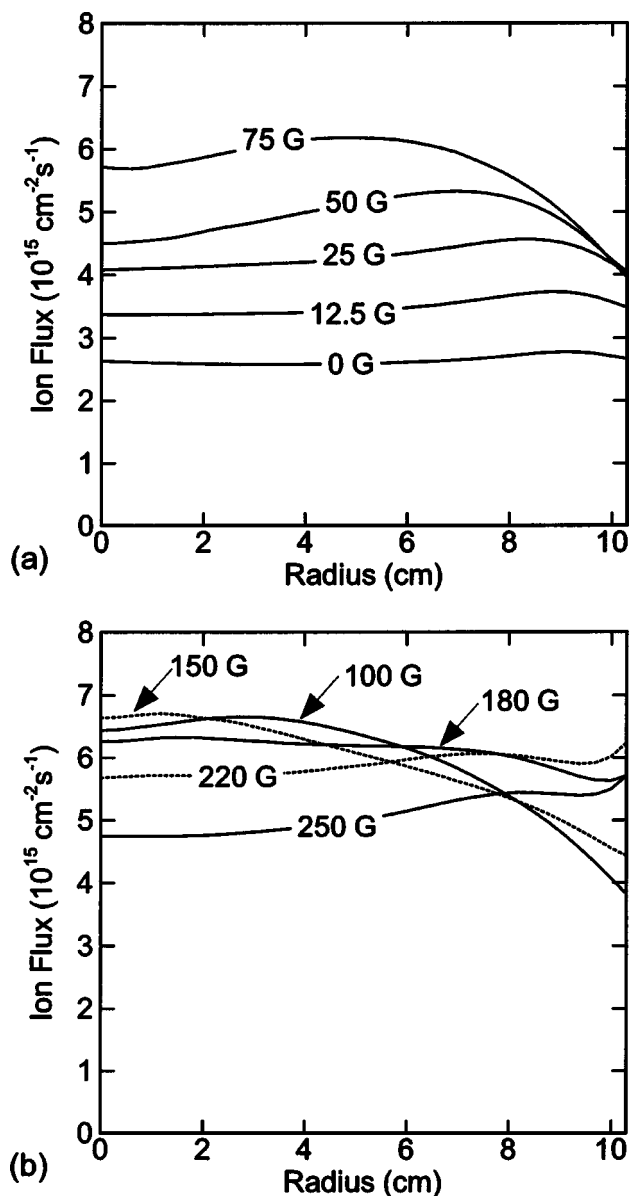
FIG. 9. Ion flux to the substrate as a function of radius for different magnetic fields (100 W, 40 mTorr): (a) 0–75 G and (b) 100–250 G. The maximum ion flux occurs at approximately 150 G.

the plasma potential profiles shown in Fig. 8. The plasma potential, $\Phi(z)$, is shown as a function of height at $r = 5$ cm at the peak of the cathodic and anodic portions of the rf cycle, and at mid-cycle, for $B = 0$, 100, and 185 G. Without a magnetic field, $\Phi(z)$ has the characteristic profile of an electropositive, highly conductive plasma, having a small voltage drop across the bulk plasma $\Phi(z)$ is always positive with respect to surfaces to confine the more mobile electrons. With moderate increases in magnetic field, which decreases the electron mobility relative to the ions, the plasma becomes more resistive, as shown by the larger voltage drop across the bulk plasma for $B = 100$ and 185 G. The discharge also loses its electropositive nature. For example, with $B = 100$ G, at which $\mu_e / \mu_I \approx 2.5$, the electric field in the powered sheath is reversed at the peak of the cathodic cycle compared to that with $B = 0$. This reversal in the electric field confines (decelerates) ions and accelerates elec-
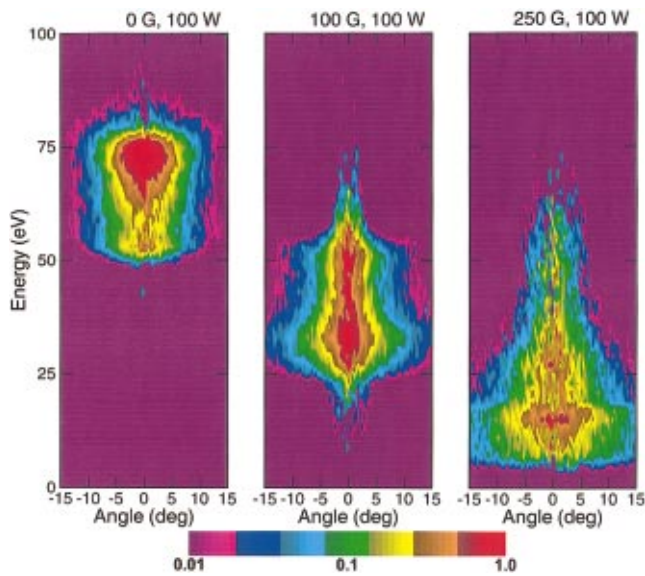
FIG. 10. (Color) IEADs striking the substrate for radii <5 cm for magnetic fields of 0, 100, and 250 G. The IEADs have units of eV^{-1} sr^{-1}. The contours span 2 decades using a log scale. The decrease in dc bias (becoming more positive) with increasing magnetic field results in low energy fluxes having broader angular distributions.
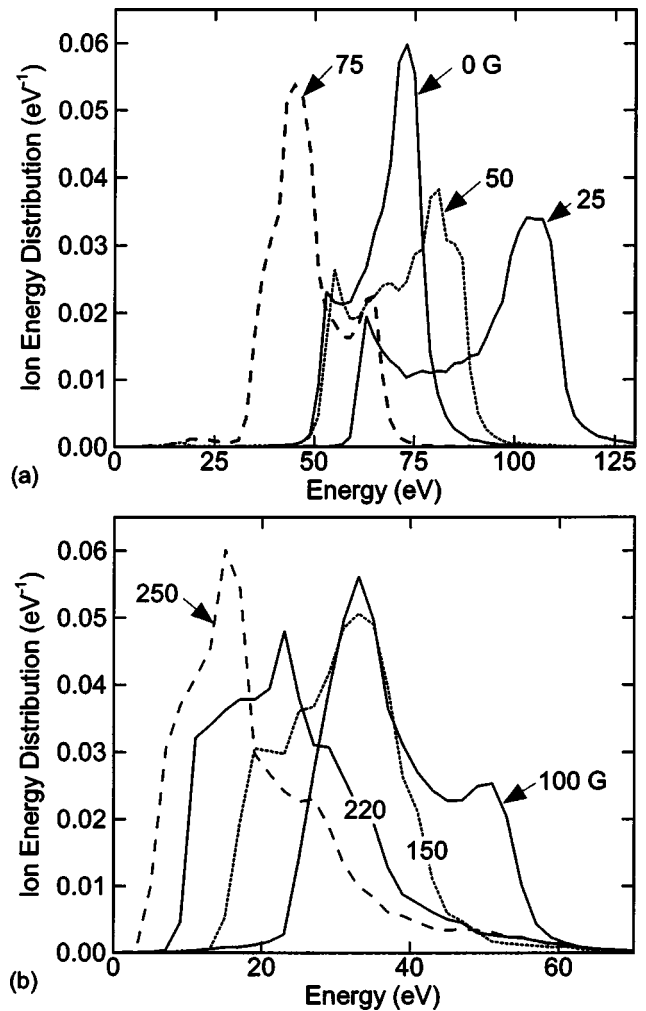

FIG. 11. Ion energy distributions integrated over angle striking the substrate for radii <5 cm for different magnetic fields: (a) 0–75 G and (b) 100–250 G.

trons. The sheath is also thicker than without the magnetic field. With $B = 185$ G, at which $\mu_e / \mu_I \approx 0.7$, the reversal of the electric fields in the sheath and voltage drop across the bulk plasma are proportionately larger. These trends for $\Phi(z)$ are essentially the same as those measured experimentally by Yeom et al., albeit in a different geometry.[10]

Of all plasma parameters, the uniformity of the ion flux depends most critically on details of the geometry such as the permittivity and placement of focus rings. For example, ion fluxes to the substrate as a function of radius are shown in Fig. 9 for different magnetic fields. Without a magnetic field, the ion flux is fairly uniform. Increasing the magnetic field at first produces an increase in magnitude which is edge high (up to 50 G) which slowly transitions to being center high at 150 G. At higher magnetic fields the ion flux profile flattens and decreases in magnitude. Due to the sensitivity of these results to small details in the geometry of the reactor, we hesitate to make general conclusions from these trends other than to acknowledge that the uniformity of ion fluxes can be controlled with moderate adjustments of the magnetic field.[8]

Due to the decrease in the time averaged values of V_P-V_{dc} and the reversal of the electric field in the powered sheath with increasing magnetic field, the ion flux incident on the substrate decreases in energy and broadens in angle. These trends are demonstrated in Fig. 10 where the ion energy and angular distributions (IEADs) for Ar^+ incident on the central 5 cm radius of the substrate are shown. Ion energy distributions integrated over angle are shown in Fig. 11. Without a magnetic field, the time averaged value of V_P-V_{dc} is 68 V, producing an ion flux largely contained in the ranges of 50–80 eV and $-10°$ to $10°$. The decrease in V_P-V_{dc} to less than 10 V when increasing the magnetic field to 250 V lowers the average ion energy to about 10 eV while extend-

ing the range of energies to 65 eV. The angular distribution is extended to $\pm 15°$.

The maximum energy of the ion flux increases with small magnetic fields which reflects the moderate increase in dc bias (more negative). For magnetic fields larger than 25 G, the peak in the ion energy distribution occurs at successively lower energies (15 eV at 250 G) while the maximum ion energy extends to energies in excess of 75 eV. These trends indicate that with increasing magnetic field the fraction of the rf cycle which the sheath potential is at its minimum value or the electric field in the sheath is reversed increases. In unmagnetized plasmas, the electron mobility is sufficiently large that the sheath potential need be at its minimum value for only a small fraction of the rf period to collect sufficient electron current to balance the ion current. As the magnetic field increases and the electron mobility decreases relative to the ions, the sheath potential must remain at its minimum value (or electric field be reversed) for a proportionally larger fraction of the rf cycle to collect the needed electron current.

Similar trends are observed while varying pressure. For example, V_{rf}, V_{dc}, and V_p-V_{dc} are shown in Fig. 12 for
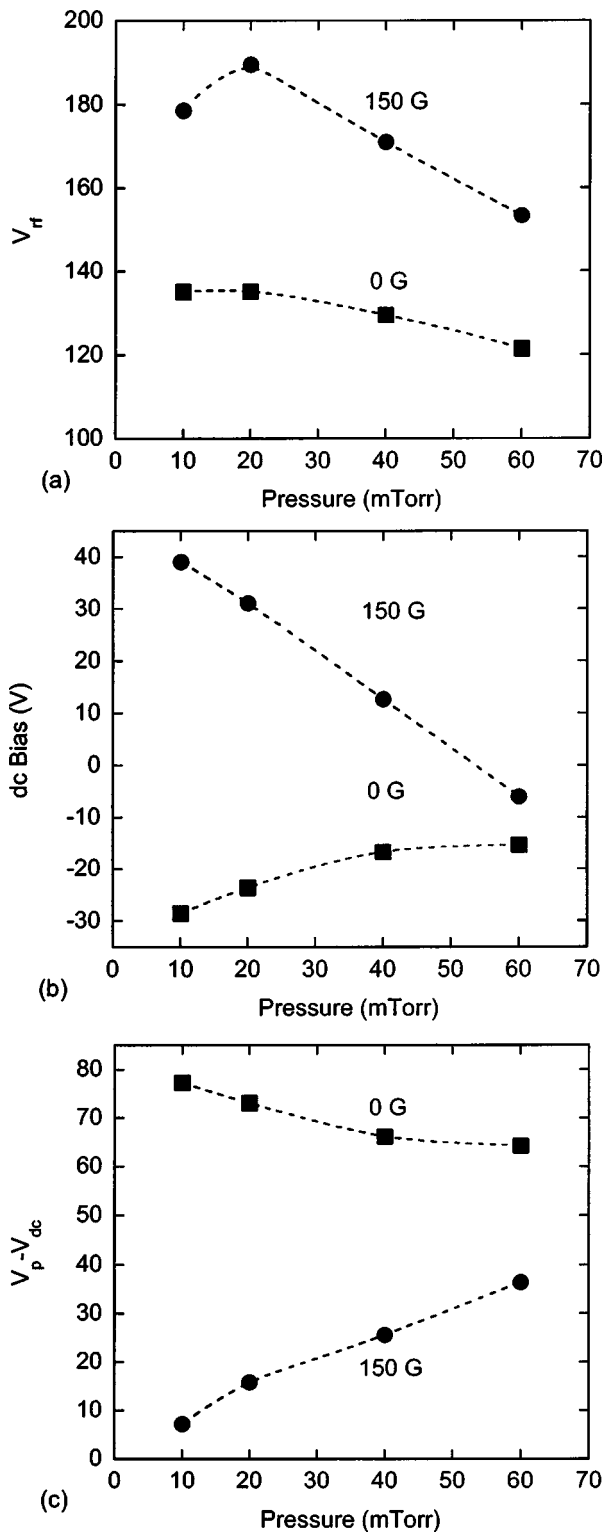
FIG. 12. Electrical parameters for a 100 W plasma with $B = 0$ and 150 G as a function of pressure: (a) rf voltage amplitude, (b) dc bias, and (c) plasma potential $-$ dc bias (V_P-V_{dc}). The trends in these quantities with decreasing pressure are similar to those for increasing magnetic field due to the decrease in electron cross field mobility.

FIG. 13. (Color) IEADs striking the substrate for radii <5 cm for magnetic fields of 0 (top) and 150 G (bottom) for pressures of 10, 20, and 60 mTorr. The IEADs have units of $eV^{-1} sr^{-1}$. The contours span 2 decades using a log scale. The decrease in dc bias (becoming more positive) with decreasing pressure results in low energy fluxes having broader angular distributions.

pressures of 10–60 mTorr without a magnetic field and with $B = 150$ G. Power deposition was held constant at 100 W. With $B = 0$, the rf amplitude moderately increases with decreasing pressure. The poorer confinement that results from higher rates of diffusi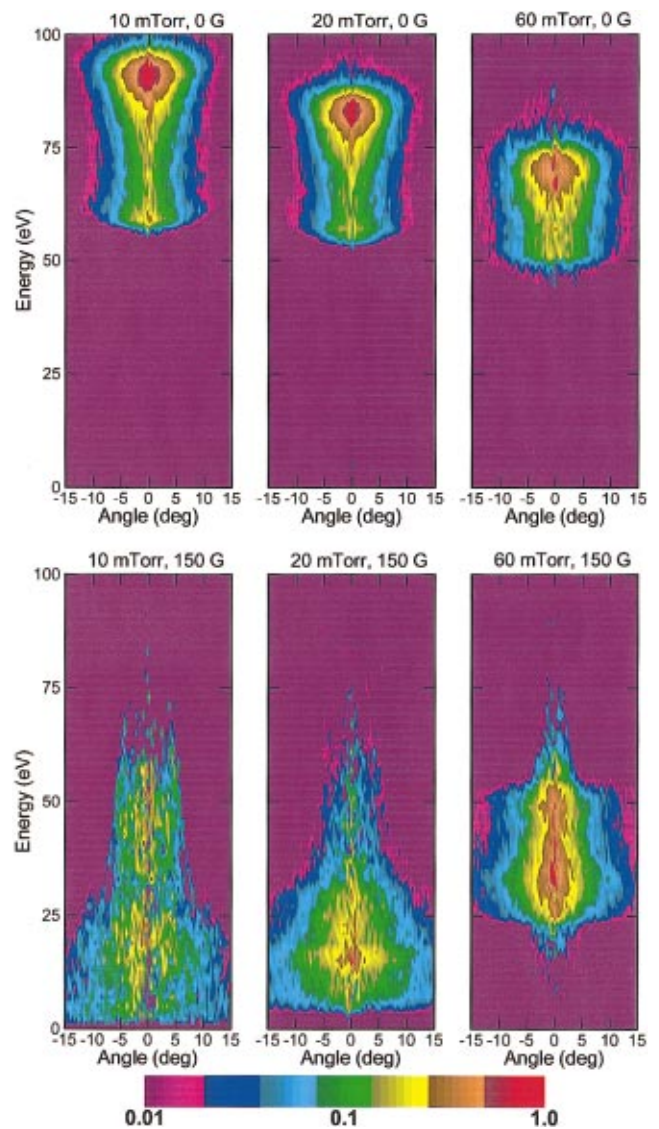on at lower pressures produce a more asymmetric discharge and more negative dc bias. With $B = 150$ G, a decrease in pressure produces more highly magnetized electrons, an increasing proportion of current carried by ions, and a larger voltage drop across the bulk plasma. The end result is more positive dc bias and smaller V_p-V_{dc}.

The consequences on the IEADs of the lower values of V_p-V_{dc} with decreasing pressure are shown in Fig. 13. IEADs are shown for pressures of 10, 20, and 60 mTorr for $B = 0$ 150 G. (See Fig. 10 for comparable results for 40 mTorr.) With $B = 0$, the mean ion energy decreases with increasing pressure in proportion to the decrease in V_p-V_{dc}. The angular distribution broadens as the sheath becomes more collisional. With $B = 150$ G, there is a severe thermalization and broadening of the IEADs with decreasing pressure as the sheath thickens and field reversal in the powered sheath occurs with the decrease in electron cross field mobility.
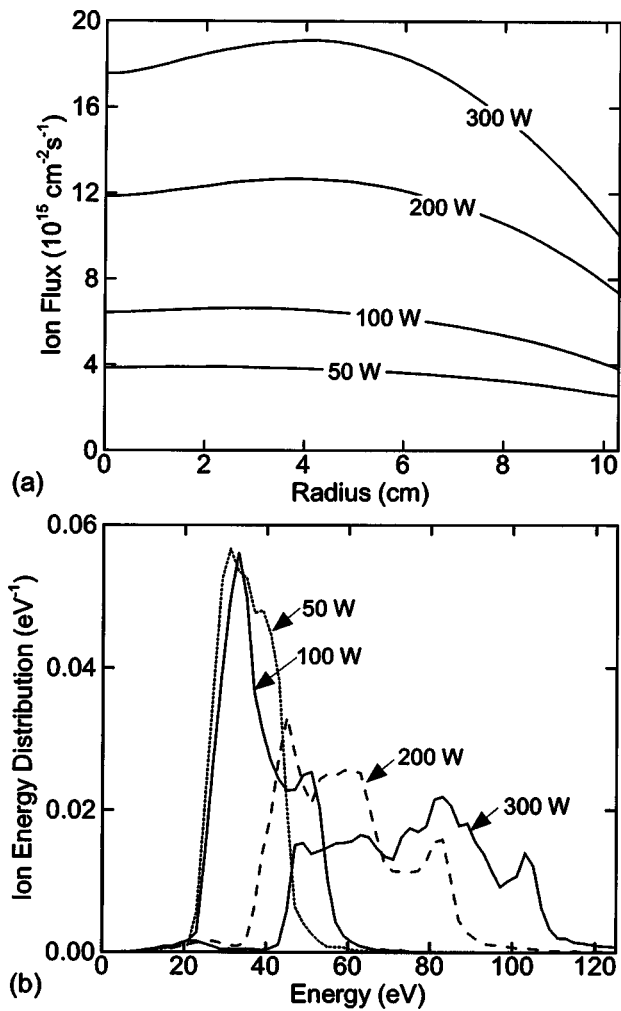
FIG. 14. Plasma parameters for a 40 mTorr plasma source with a 100 G magnetic field while varying power: (a) ion flux to the substrate as a function of radius and (b) ion angular distribution integrated over angle.
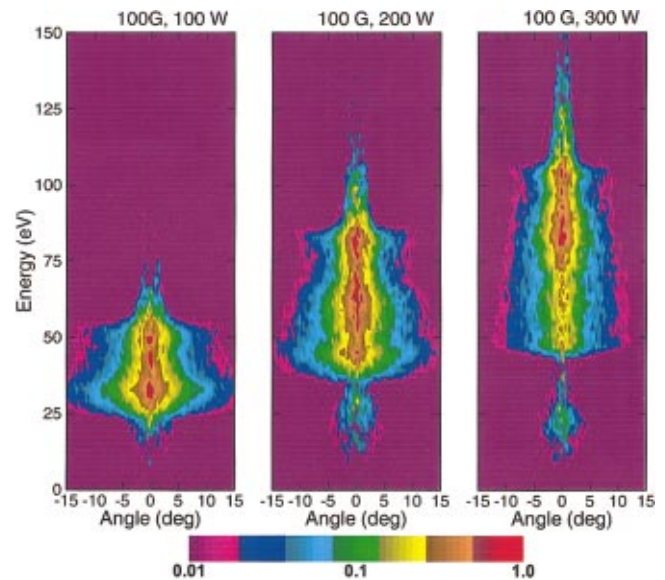

FIG. 15. (Color) IEADs striking the substrate for radii <5 cm for a magnetic fields 100 G and powers of 100, 200, and 300 W. The IEADs have units of eV^{-1} sr^{-1}. The contours span 2 decades using a log scale. Although the larger rf amplitude and larger dc bias (more negative) with increasing power produces a more extended ion energy distribution, the residual low energy component persists.

Ion fluxes as a function of radius and energy, and IEADs are shown in Figs. 14 and 15 while varying power deposition from 50 to 300 W for a magnetic field of 100 G. The increase in rf amplitude over this increase in power is 126–213 V, and the change in dc bias is -13 to -36 V. The increases in ion flux with power are less than linear as a consequence of an increasing proportion of the power being dissipated by ion acceleration. The ion flux becomes increasingly nonuniform with increasing voltage, a trend which is shared with conventional capacitive discharges.[23] As the power and voltage increase, the sheath thickness increases, thereby also increasing the ion transit time. The end result is more structure in the ion energy distribution. In spite of the sheath thickening, the increase in sheath potential produces a narrowing of the ion angular distribution. The persistence of the low energy component of the ion energy distribution reflects the large fraction of the rf period at which the sheath potential is near its minimum value or electric field is reversed.

IV. CONCLUDING REMARKS

The properties of MERIE plasma sources sustained in argon have been computationally investigated using results from a two-dimensional plasma transport model. Experimentally observed trends of decreasing dc bias (more positive), localization of plasma density near the powered electrode and reversal of the electric field in the powered sheath with increasing magnetic field are reproduced with the model. These trends are attributed to the reduction in cross field mobility of electrons resulting in a more resistive plasma and more current being carried by ions. The ranges of secondary electrons emitted by surfaces and accelerated by the sheaths are also reduced, thereby contributing to localizing ionization sources near the powered electrode. As electron impact sources are localized near the powered electrode with increasing magnetic field, the maximum in neutral excited state densities also move towards the substrate. Since neutral transport is not directly affected by the magnetic field diffusion losses increase, producing a disproportionate decrease in excited state densities and multistep ionization. As the magnetic field increases and electron mobility decreases the proportion of the rf cycle during which the sheath potential is at its minimum value increases, and in some cases the electric field reverses. This trend contributes to decreasing the energy of the ion flux incident onto the substrate.

[1] R. A. Lindley, C. H. Bjorkman, H. Shan, K.-H. Ke, K. Doan, R. R. Mett, and M. Welch, J. Vac. Sci. Technol. A **16**, 1600 (1998).

[2] K. E. Davies, M. Gross, and C. M. Horwitz, J. Vac. Sci. Technol. A **11**, 2752 (1993).

[3] M. J. Buie, J. T. P. Pender, and P. L. G. Ventzek, Jpn. J. Appl. Phys., Part 1 **36**, 4838 (1997).

[4] P. Berruyer, F. Vinet, H. Feldis, R. Blanc, M. Lerme, Y. Morand, and T. Poiroux, J. Vac. Sci. Technol. A **16**, 1604 (1998).

[5] C. T. Gabriel, J. Vac. Sci. Technol. B **20**, 1542 (2002).

[6] C. O. Jung, K. K. Chi, B. G. Hwang, J. T. Moon, M. Y. Lee, and J. G. Lee, Thin Solid Films **341**, 112 (1999).

[7] M. J. Buie, J. T. P. Pender, and M. Dahimene, J. Vac. Sci. Technol. A **16**, 1464 (1998).

[8] A. P. Paranjipe, M. M. Moslehi, and C. J. Davis, J. Vac. Sci. Technol. A **10**, 1140 (1992).

[9] G. Y. Yeom, J. A. Thornton, and M. J. Kushner, J. Appl. Phys. **65**, 3816 (1989).

[10] G. Y. Yeom, J. A. Thornton, and M. J. Kushner, J. Appl. Phys. **65**, 3825 (1989).

[11] D. A. W. Hutchinson, M. M. Turner, R. A. Doyle, and M. B. Hopkins, Trans. Plasma Sci. **23**, 636 (1995).

[12] S. V. Avtaeva, M. Z. Manytbekov, and D. K. Otorbaev, J. Phys. D **30**, 3000 (1997).

[13] J-C. Park and B. Kang, Trans. Plasma Sci. **25**, 499 (1997).

[14] M. A. Lieberman, A. J. Lichtenberg, and S. E. Sava, Trans. Plasma Sci. **19**, 189 (1991).

[15] X. Xu, S. Rauf, and M. J. Kushner, J. Vac. Sci. Technol. A **18**, 213 (2000).

[16] P. A. Thompson, *Compressible-Fluid Dynamics* (McGraw-Hill, New York, 1972), p. 98.

[17] S. D. Rockwood, Phys. Rev. A **8**, 2348 (1973).

[18] P. Subramonium and M. J. Kushner, J. Vac. Sci. Technol. A **20**, 313 (2002).

[19] DSLUCS obtained from the SLAP Sparse Matrix Library available from the Oak Ridge National Laboratory NETLIB Archive (http://www.netlib.org).

[20] R. L. Kinder and M. J. Kushner, J. Appl. Phys. **90**, 3699 (2001).

[21] J. Lu and M. J. Kushner, J. Vac. Sci. Technol. A **19**, 2652 (2001).

[22] J. R. Roberts, J. Res. Natl. Inst. Stand. Technol. **100**, 353 (1995).

[23] G. A. Hebner and K. E. Greenberg, J. Res. Natl. Inst. Stand. Technol. **100**, 373 (1995).